ACS APPLIED MATERIALS & INTERFACES

Research Article

www.acsami.org

Ionic Conductivity of Mesostructured Yttria-Stabilized Zirconia Thin Films with Cubic Pore Symmetry—On the Influence of Water on the Surface Oxygen Ion Transport

Matthias T. Elm,*[,†,‡] Jonas D. Hofmann,[†] Christian Suchomski,[†,§] Jürgen Janek,[†] and Torsten Brezesinski*[,§]

[†]Institute of Physical Chemistry, Justus-Liebig-University Giessen, Heinrich-Buff-Ring 58, 35392 Giessen, Germany

[‡]Institute of Experimental Physics I, Justus-Liebig-University Giessen, Heinrich-Buff-Ring 16, 35392 Giessen, Germany

[§]Institute of Nanotechnology, Karlsruhe Institute of Technology, Hermann-von-Helmholtz Platz 1, 76344 Eggenstein-Leopoldshafen, Germany

Supporting Information

ABSTRACT: Thermally stable, ordered mesoporous thin films of 8 mol % yttria-stabilized zirconia (YSZ) were prepared by solution-phase coassembly of chloride salt precursors with an amphiphilic diblock copolymer using an evaporation-induced self-assembly process. The resulting material is of high quality and exhibits a well-defined three-dimensional network of pores averaging 24 nm in diameter after annealing at 600 °C for several hours. The wall structure is polycrystalline, with grains in the size range of 7 to 10 nm. Using impedance spectroscopy, the total electrical conductivity was measured between 200 and 500 °C under ambient atmosphere as well as in dry atmosphere for oxygen partial pressures ranging from 1 to 10^{-4} bar. Similar to bulk YSZ, a constant ionic conductivity is observed over the whole oxygen partial pressure range investigated. In dry atmosphere, the sol–gel derived films have a much higher conductivity, with different activation energies for low and high temperatures. Overall, the results indicate a strong influence of the surface on the transport properties in cubic fluorite-type YSZ with high surface-to-volume ratio. A qualitative defect model which includes surface effects (annihilation of oxygen vacancies as a result of water adsorption) is proposed to explain the behavior and sensitivity of the conductivity to variations in the surrounding atmosphere.

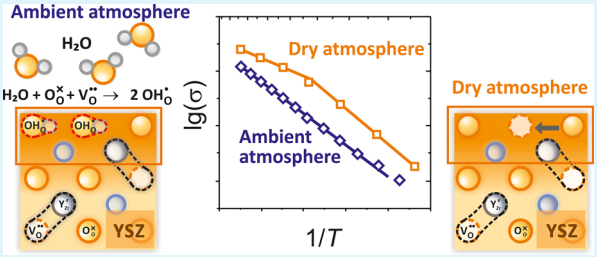

KEYWORDS: *yttria-stabilized zirconia, nanoionics, proton conductivity, surface effects, self-assembly, mesoporous*

INTRODUCTION

Oxygen ion conductors are of great interest as solid electrolytes in numerous research areas and applications, such as solid oxide fuel cells,[1−3] gas sensors,[4] and ionic membranes.[5,6] Perhaps the most prominent oxygen ion conductor is yttria-stabilized zirconia (YSZ). YSZ has good ionic conductivity at elevated temperatures and further boasts high chemical and mechanical stability.[7,8] The acceptor doping with yttrium not only stabilizes the cubic fluorite-type phase but also results in the formation of oxygen vacancies. These vacancies are responsible for the ionic transport properties.[7] However, for most technical applications, the ionic conductivity at intermediate temperatures is not sufficient, thus making it necessary to find ways of increasing it.[2,9,10]

An obvious strategy for improving the ionic conductivity of solid electrolytes is nanostructuring, that is, altering the morphology and grain size.[11,12] Following this strategy, enhancements in ionic conductivity of YSZ thin films by up to 2 orders of magnitude have been reported and attributed to (1) reduction of the grain boundary resistance,[13−15] (2) strain effects and/or misfit dislocations,[16−18] or (3) higher oxygen diffusivity at the film/substrate interface.[19] But still, there are also reports of no enhancement[20,21] and sometimes even a decrease in ionic conductivity has been observed.[22,23] As a result there is a wide range of values for the conductivity of nanoscale YSZ.[12] The major reason for the divergent findings is the difficulty of controlling both the chemical composition and microstructure of the grain boundaries in polycrystalline ceramics. The concept of nanostructuring of solid electrolytes has also attracted the attention of many researchers due to the prospect of enhancing the proton conductivity at low temperatures. Although this effect has been observed in several nanocrystalline materials,[24−28] its origin and the impact of grain boundaries, grain size, and porosity is still under debate.[26,29−31]

The conductivity of YSZ thin films is usually measured laterally, with electrodes attached to the top surface. By decreasing the film thickness to the nanoscale, the surface contribution to the overall behavior becomes more and more

Received: February 2, 2015
Accepted: May 18, 2015
Published: May 18, 2015

DOI: 10.1021/acsami.5b01001
ACS Appl. Mater. Interfaces 2015, 7, 11792−11801

important—in parallel to the influence of the film/substrate interface. Because the surface region can show different physical properties than the bulk, surface effects may play a crucial role in the study of ionic transport processes in nanometer thick films. This has been recently highlighted in a review by Korte et al.[32]

Mesoporous materials having both a close-packed arrangement of interconnected sub-50 nm diameter pores represent an ideal model system to study surface effects—without the disturbing influence of heterophase solid/solid interfaces. The electrochemical properties of such materials are strongly affected by the high surface-to-volume ratio resulting from the mesoporous structure which, among others, provides easy access to single grains in the walls.[33−35]

Here, we describe the transport properties of cubic mesoporous thin films of 8 mol % yttria-stabilized zirconia as a function of temperature and oxygen partial pressure. While a behavior similar to microcrystalline (bulk) films is observed in ambient atmosphere, the sol−gel derived material shows significant changes in the transport properties in dry atmosphere, with two activation energies in the temperature range from 200 to 500 °C. These results can qualitatively be explained by a dominating surface conduction mechanism, which is strongly affected by adsorbed water.

EXPERIMENTAL SECTION

Mesoporous thin films of 8 mol % yttria-stabilized zirconia were prepared by evaporation-induced self-assembly (EISA).[36−38] In brief, an ethanolic solution containing both sol−gel precursors (namely, $YCl_3 \cdot 6H_2O$ and $ZrCl_4$) and an amphiphilic diblock copolymer structure-directing agent (here, $H[C(CH_3)_2CH_2]_{107}C_6H_4(OCH_2CH_2)_{150}OH$, PIB_{107}-*b*-PEO_{150})[39,40] was deposited onto either a quartz glass substrate or silicon wafer by dip-coating. Optimal conditions include relative humidities ranging from 15 to 20% and constant withdrawal rates of 1 to 10 mm/s. After deposition, the films were dried for 1 h at 130 °C to stabilize the nanostructure and then heated to 600 °C using a 94 min ramp, followed by aging for 10 h. The latter high temperature treatment results in complete combustion of the polymer template and crystallization of the YSZ framework.

Scanning electron microscopy (SEM) images were collected on a MERLIN from Carl Zeiss at 5 keV. Transmission electron microscopy (TEM) images were taken using an FEI Titan 80−300 electron microscope operated at 300 keV in TEM mode for HRTEM and in nanoprobe mode for STEM imaging. Wide-angle X-ray diffraction (WAXD) was carried out on an X'Pert PRO from PANalytical instruments (λ = 0.15418 nm) with X'Celerator RTMS detector. Time-of-flight secondary ion mass spectrometry (ToF-SIMS) measurements were performed using a TOF-SIMS 5 from ION-TOF GmbH. The analysis beam was Bi^+ (25 keV, 1.46 pA, 100 · 100 μm^2) and the etching beam was O_2^+ (1 keV, 249.85 pA, 200 · 200 μm^2). Raman spectra were collected on a SENTERRA dispersive Raman microscope from Bruker Optics with Olympus objective MPlan N 100x and a Nd:YAG laser. Grazing incidence small-angle X-ray scattering (GISAXS) experiments were carried out at beamline BW4 of the German synchrotron radiation facility HASYLAB at DESY (λ = 1.381 Å, $d_{sample/detector}$ = 1805 mm, β = 0.2°) using a MarCCD area detector (79 μm pixel size, counting time = 2 · 300 s). *DPDAK* version 1.0.0 was used for data analysis.

The total electrical conductivity of the mesoporous thin films was measured by impedance spectroscopy in the frequency range from 1 mHz to 1 GHz with a voltage of 500 mV using a Novocontrol Alpha-A measuring bridge. Two interdigitated Pt microelectrodes were prepared on the top surface of the films by photolithography. At first, negative resist (ma-N 1420, micro resist technology GmbH) with a thickness of about 2 μm was deposited onto the samples. After a prebake for 100 s at 120 °C, the electrode structure was transferred using a chrome-plated soda lime glass mask and a mask aligner (MA56, Karl Süss) operating at 365 nm. After development (maD 533-S, micro resist technology GmbH), a hard bake at 100 °C for 45 min was performed. A 200 nm thick Pt electrode was then deposited by pulsed laser deposition using a Pt target and a KrF excimer laser (248 nm). For the lift-off process, acetone was used. The microelectrodes have an accumulated length of 40 cm and an electrode distance of 20 μm. A schematic illustration of the interdigitated electrodes is shown in Figure S1 of the Supporting Information (SI).

The in-plane resistance was measured in the temperature range from 200 to 500 °C inside a gastight tube furnace. The temperature was controlled using a type K thermocouple and a digital multimeter 2700 (Keithley) with a reference junction at 50 °C. The oxygen partial pressure was controlled by mixtures of Ar and O_2 and measured using a home-built zirconia-based EMF cell and a digital multimeter 2700 (Keithley). The gas mixture was dried over $CaCl_2/P_2O_5$ before flowing into the tube furnace. For the temperature-dependent measurements at ambient atmosphere, the tube furnace was kept open. Before each temperature and $p(O_2)$-measurement step, the sample was allowed to equilibrate for 6 to 10 h.

RESULTS AND DISCUSSION

The YSZ thin films studied in this work were prepared by sol−gel dip-coating[37,38] using chloride salt precursors and a large polyisobutylene-*block*-poly(ethylene oxide)[39,40] diblock copolymer as structure-directing agent. In so doing, the best result in terms of pore ordering and material homogeneity was achieved.

Both the surface and bulk morphology of the solution-processed material after annealing at 600 °C for 10 h were investigated by electron microscopy. Representative top view and cross-sectional SEM images are shown in Figure 1a,b and

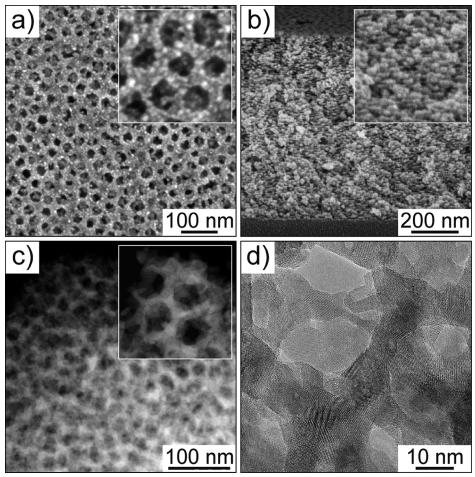

Figure 1. Electron microscopy of the polymer-templated mesostructured YSZ thin films heated at 600 °C for 10 h. Top view (a) and cross-sectional SEM images (b), and HAADF-STEM images (c) showing that the network of pores is well developed. The side lengths of the high magnification images in the inset are 125 nm (a), 235 nm (b), and 90 nm (c). (d) HRTEM image demonstrating the high crystallinity.

SI Figure S2. As can be seen, the films have a continuous mesostructure with distorted cubic pore symmetry. The average size of the cavities is 24 nm in plane. The dimension in the direction normal to the plane of the substrate is much smaller because of the unidirectional film contraction during thermal annealing. In addition, it is evident from the SEM images that the pores at the top surface are open, the nanoscale structure persists throughout the bulk, and that even several hundred

DOI: 10.1021/acsami.5b01001
ACS Appl. Mater. Interfaces 2015, 7, 11792−11801

nanometer thick layers of YSZ are crack-free on the micrometer level. This is also corroborated by the high-angle annular dark-field scanning transmission electron microscopy (HAADF-STEM) images in Figure 1c. Both high-resolution TEM (Figure 1d) and selected-area electron diffraction (see SI Figure S2) demonstrate the polycrystalline nature of the wall structure; no amorphous regions were observed. Overall, the electron microscopy data verify the high quality of the YSZ thin films with minor structural defects. There are no signs of restructuring or instability at 600 °C which emphasizes the exceptional thermal stability of the sol–gel derived material.

The pore structure and its thermal stability were also investigated by means of synchrotron-based GISAXS. Figure 2

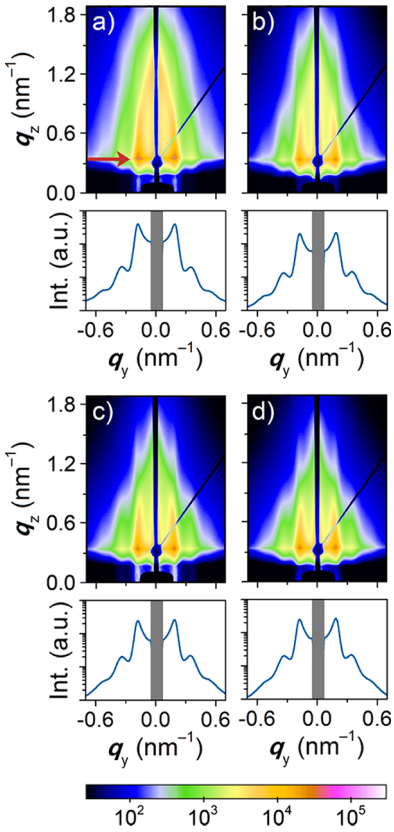

Figure 2. GISAXS patterns of the mesoporous nanocrystalline YSZ thin films heated at 600 °C for 1 min (a), 1 h (b), 10 h (c), and 50 h (d). The angle of incident β was set at 0.2°. The intensity color map is shown at the bottom. Line cuts made along the direction indicated by the red arrow in (a) are shown below the GISAXS patterns.

shows GISAXS patterns obtained on a sub-200 nm thick film heated at 600 °C for different times. Strong in- and out-of-plane maxima, characteristic of a distorted large-pore cubic mesophase with reasonable ordering, can be observed after annealing for up to 1 h.[35,40] The corresponding patterns indicate lattice contraction (perpendicular to the substrate) of more than 80%. The scattering intensity loss in the q_z-direction for longer annealing times can be attributed to the morphological anisotropy of the films. However, the maxima in the q_y-direction are preserved, thereby demonstrating that the lateral pore structure is little affected. This can also be seen from the horizontal line cuts in Figure 2. Even higher order maxima are clearly visible after 50 h at 600 °C.

The crystallite size was determined by X-ray diffraction. WAXD patterns as a function of annealing time at 600 °C are shown in Figure 3a. Distinct (111) and (200) peaks at 2θ values of 30.2° and 35.0°, respectively, can be observed. As is evident, the YSZ thin films are already highly crystalline after annealing for only 1 min and the line broadening of the peaks barely changes with time. Applying the Scherrer equation to the (111) peak gives an average crystallite size of 8 nm, which is of the order of the wall thickness. This result thus provides an explanation as to why the pore structure remains virtually unaffected; phenomena like sintering or gain growth are not observed.

The polymer-templated mesostructured films were also characterized using Raman spectroscopy, ToF-SIMS, and XPS. The Raman spectrum shows only a single line at about 610 cm^{-1} (see SI Figure S3). This band can be assigned to an F_{2g} mode and is characteristic of the cubic fluorite-type phase.[41] Figure 3b shows the depth profiling results from positive polarity ToF-SIMS analysis. Both the $^{89}Y^+$ and $^{91}Zr^+$ signals are constant until the film/substrate interface is reached, which demonstrates that the Y and Zr ions are homogeneously distributed throughout the depth. The surface composition and bonding were investigated by XPS. A survey scan confirming the absence of any contaminants is shown in SI Figure S4, detail spectra of the Y 3d and Zr 3d core levels are illustrated in Figure 3c,d. The latter spectra can be fitted to two peaks, with an area ratio of 2:3 and low χ^2 values, at 159.04 eV (Y^{3+})/184.38 eV (Zr^{4+}) and 157.00 eV (Y^{3+})/182.00 eV (Zr^{4+}) due to emissions from the $3d_{3/2}$ and $3d_{5/2}$ components, respectively. XPS further indicates nearly perfect 1:5.25 Y/Zr stoichiometry (Y/Zr/O atomic ratio 1:5.27:12.14). Taken together, the data in Figure 3 establish that the mesoporous YSZ thin films are single phase and well-defined—they are an ideal model system with which to study the effect of free surface on the ionic transport properties.

Figure 4 shows a comparison of representative impedance spectra of ~150 nm thick mesoporous YSZ films measured at two temperatures under ambient atmosphere and in dry air with both ambient and low oxygen partial pressures. All spectra show a nearly ideal semicircle at high frequencies in the range between 1 MHz and 100 Hz, and further the onset of one or two semicircles at low frequencies. For the measurements at high temperatures and ambient atmosphere especially, the appearance of a third semicircle can be observed. This semicircle shifts to lower frequencies with decreasing temperature, becomes more and more depressed and eventually disappears below 700 K. In dry air conditions, it is less pronounced and merges with the second semicircle. It is worth noting that a bare quartz glass substrate was also measured to assess the effect of potential leakage currents. As shown in SI Figure S5, the resistance of the substrate is about 4 orders of magnitude larger than that of the YSZ thin films, and therefore leakage can be ruled out.

In order to analyze the impedance spectra and to determine the resistance of the films, the data were fitted using an equivalent circuit consisting of *RQ* elements in series. At high temperatures and ambient atmosphere (three semicircles appeared), three *RQ* elements were used; the impedance spectra with two semicircles were fitted using an equivalent circuit with only two *RQ* elements. Each of the *RQ* elements represents one of the corresponding nonideal semicircles with resistance R_i and constant phase element Q_i. The fits to the data are shown as solid lines in Figure 4. From the parameters *n* and

DOI: 10.1021/acsami.5b01001
ACS Appl. Mater. Interfaces 2015, 7, 11792–11801

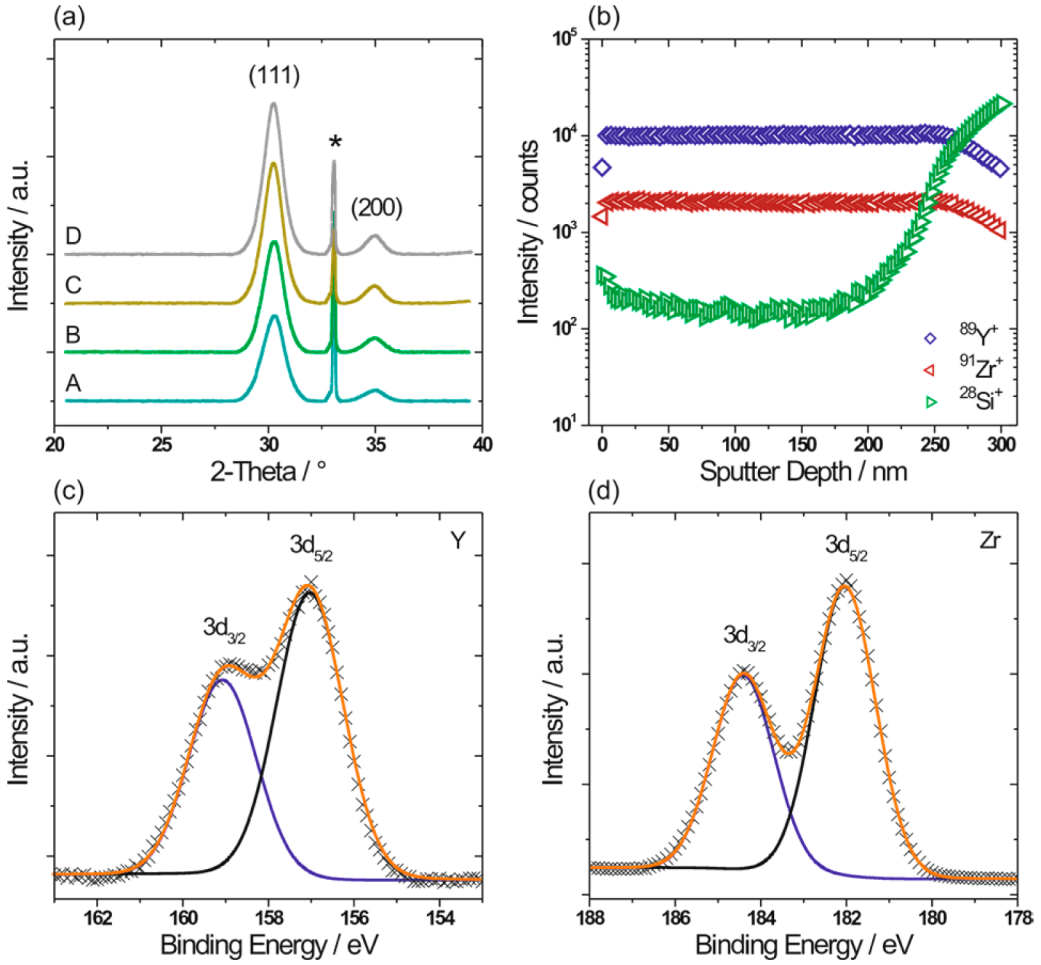

Figure 3. (a) WAXD patterns of the mesoporous YSZ thin films heated at 600 °C for 1 min (A), 1 h (B), 10 h (C), and 50 h (D). The peak denoted with an asterisk mark stems from the silicon wafer used as substrate. (b) ToF-SIMS depth profiling of a ~250 nm thick film. (c, d) XPS detail spectra of the Y 3d and Zr 3d levels. Experimental data are shown as diagonal crosses, lines in black and blue are fits to the data and orange lines represent the sum of the peak fits.

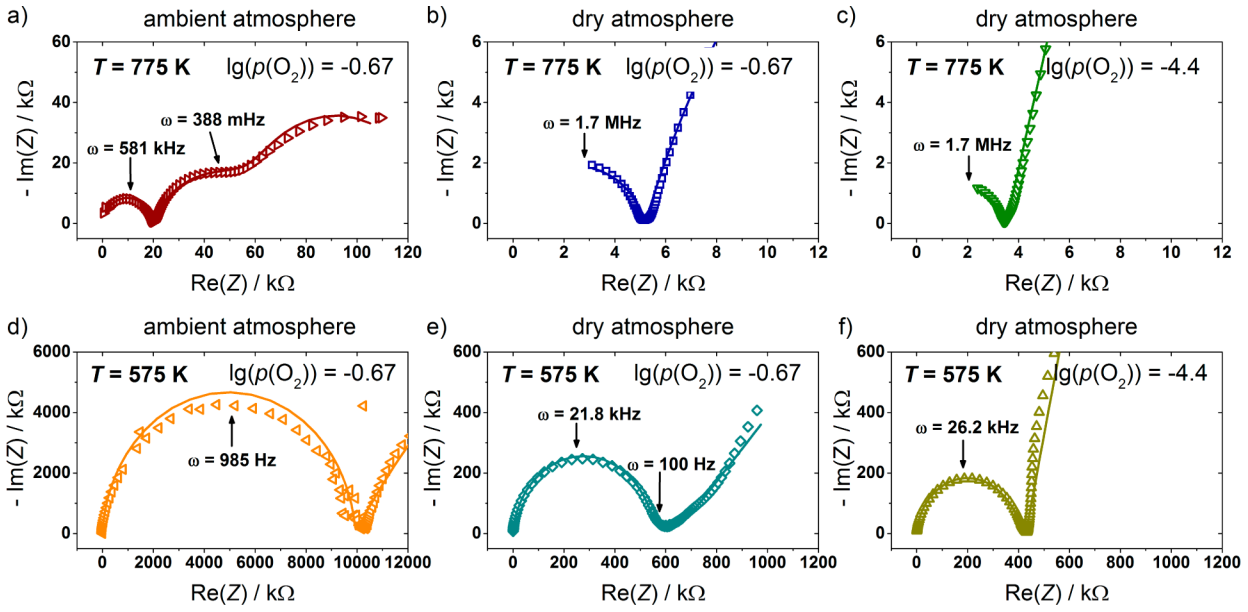

Figure 4. Complex impedance spectra of the mesoporous YSZ thin films measured at high (top) and low (bottom) temperatures and under ambient atmosphere (left) as well as in dry air with ambient oxygen partial pressure (middle) and low oxygen partial pressure (right). Simulated impedance spectra are shown as solid lines.

DOI: 10.1021/acsami.5b01001
ACS Appl. Mater. Interfaces 2015, 7, 11792−11801

C_Q of the constant phase element, the capacitance C_i of the semicircles can be calculated according to the following:[42,43]

$$C = R^{1-n}C_Q^{1/n} \quad (1)$$

For the semicircle at high frequencies, a capacitance of about 1.2×10^{-13} F was determined. For those at low frequencies, values of 1×10^{-6} to 1×10^{-5} F were found. The semicircle at high frequencies can therefore be attributed to the response of the electrolyte, while those at low frequencies correspond to the response of the electrode/electrolyte interface.[44] This interpretation is also supported by impedance measurements at different bias voltages (not shown). Only the two semicircles at low frequencies are affected by variations in applied voltage, as expected for electrode processes. As we focus here on the electrolyte properties, we did not investigate the electrode/electrolyte response in detail. In the following sections, we take a closer look at the resistance of the electrolyte.

Using the resistance determined from the impedance spectra, the conductivity of the mesoporous YSZ thin films was calculated according to the following:

$$\sigma = \frac{1}{R}\frac{l}{bd} \quad (2)$$

where R represents the resistance, l the electrode distance, b the electrode length, and d is the film thickness. However, this way the conductivity of the mesoporous YSZ is underestimated because the porosity is neglected. The electrode area $b \times d$ would be reduced when considering the pore structure, ultimately leading to an increase of the geometrical factor and therefore to a higher conductivity. But since it is very difficult to determine the exact geometrical correction term, the samples were treated as dense films. Consequently, the total conductivity determined by eq 2 could be the bottom limit of the conductivity of the material. The temperature dependence of the conductivity in ambient atmosphere as well as in dry atmosphere for the lowest and highest oxygen partial pressures tested is shown in Figure 5.

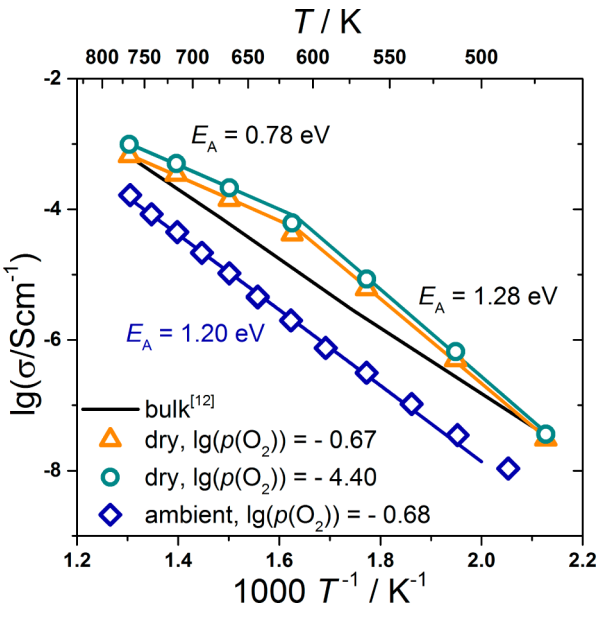

Figure 5. Temperature dependence of the conductivity for different atmospheric conditions. The black line is the average of reported values for bulk YSZ taken from ref.[12]

The conductivity in ambient atmosphere reveals linear behavior, with Arrhenius-type dependence over the whole temperature range. A fit of the experimental data to the expression $\ln(\sigma T) = \ln(\sigma_0) - E_A/k_BT$ gave an activation energy of 1.20 eV. This value is comparable to those reported for single crystals of YSZ and polycrystalline bulk material. Typical values lie between 0.8 and 1.23 eV.[21,22,45−48] For comparison, the average of the conductivity values for bulk YSZ taken from ref 12 is shown in Figure 5 as well. Apart from the agreement between the activation energies, the absolute value of the total conductivity of mesoporous YSZ is lower by about 1 order of magnitude compared to its bulk-phase counterpart. One should keep in mind, nevertheless, that the mesoporous samples were considered as dense films in the calculation. This means the bulk conductivity of the crystallites is underestimated to a certain extent.

Measurements in dry atmosphere show a distinct change in the conductivity behavior. As is evident from Figure 5, the absolute value of the conductivity increases by approximately 1 order of magnitude under dry conditions and ambient oxygen partial pressure ($\lg(p(O_2)/\text{bar}) = -0.67$), reaching values even higher than those typically observed for bulk YSZ. In addition, the temperature dependence of the conductivity shows two transport regimes with different activation energies. For temperatures below 630 K, a slightly increased activation energy of about 1.28 eV is deduced, while a significant decrease of E_A to 0.78 eV is found at higher temperatures. Furthermore, the data do not show notable changes with variations in the oxygen partial pressure. The absolute values of the total conductivity are virtually constant for the oxygen partial pressure range investigated (here, $\lg(p(O_2)/\text{bar}) = -0.67$ to -4.4), as can be seen in Figure 6. The same also holds true for the activation energy at low and high temperatures—E_A is shown as a function of oxygen partial pressure in Figure 7.

The intrinsic metastability of mesoporous materials may lead to the fact that they undergo structural and/or morphological changes,[49] especially at high temperatures, due to sintering or other causes. In order to ascertain that the differences in conductivity are not caused by such changes, all measurements were repeated several times. The same behavior was observed

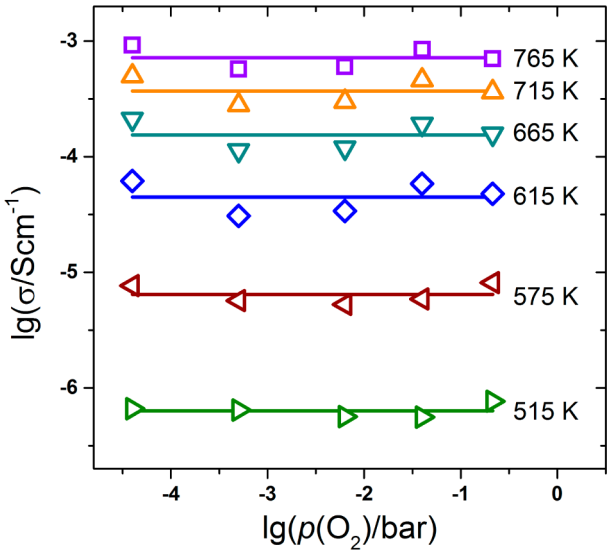

Figure 6. $p(O_2)$ dependence of the total conductivity measured at different temperatures. Solid lines are fits to the experimental data.

DOI: 10.1021/acsami.5b01001
ACS Appl. Mater. Interfaces 2015, 7, 11792−11801

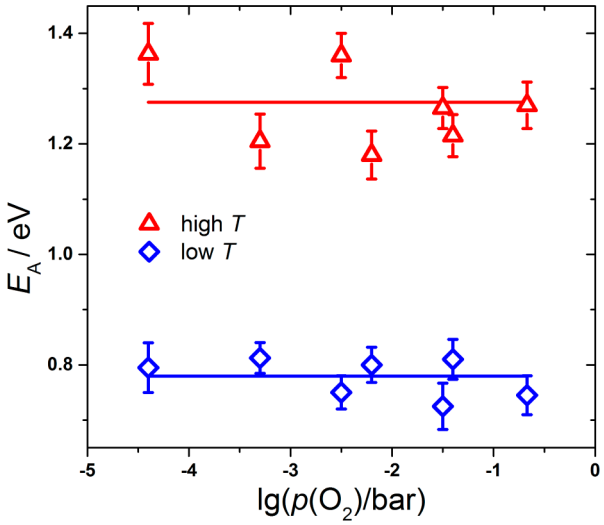

Figure 7. $p(O_2)$ dependence of the activation energy at low and high temperatures. Solid lines are fits to the experimental data.

in each of the measurements, which provides ample evidence that the change in conductivity is reversible and only depends on the atmospheric conditions. In addition, SEM confirmed that the mesoporous morphology is fully preserved.

In order to explain the different temperature dependence of the ionic conductivity in dry and ambient environments, one has to consider the underlying transport mechanism in the mesoporous YSZ thin films. In bulk oxide ceramics with a fluorite-type structure, such as CeO_2 and ZrO_2, the conductivity is determined by the defect concentration of mobile electronic and ionic charge carriers. This means it depends on the electronic band gap and the anion Frenkel defect equilibrium. The defect concentration and thus the electrical properties can be altered by either doping or varying the oxygen partial pressure in the surrounding gas phase.

According to the well-established defect model for YSZ, the doping with yttrium results in the formation of oxygen vacancies for charge compensation. Using Kroeger-Vink notation, the doping can be described as follows:[45,50]

$$Y_2O_3 \xrightarrow{ZrO_2} 2Y'_{Zr} + V^{\cdot\cdot}_O + 3O^x_O \quad (3)$$

where Y'_{Zr} denotes an Y^{3+} impurity located at a Zr^{4+} site with relative charge of −1, and $V^{\cdot\cdot}_O$ represents an oxygen vacancy with relative charge of +2. Oxygen vacancies are also generated under reducing conditions as oxygen will be released from the lattice according to the following defect reaction:

$$O^x_O \rightleftharpoons \frac{1}{2}O_{2(g)} + V^{\cdot\cdot}_O + 2e' \quad (4)$$

Applying the law of mass action, the mass action constant for low oxygen partial pressure can be written as follows:

$$K_{Red} = [V^{\cdot\cdot}_O][e']^2 p(O_2)^{1/2} \quad (5)$$

The electroneutrality condition at low $p(O_2)$ is then given by $2[V^{\cdot\cdot}_O] = [Y'_{Zr}] + [e']$. Because of the incorporation of 8 mol % yttria, $[Y'_{Zr}]$ is much larger than $[e']$. Therefore, the oxygen vacancy concentration can be considered constant in reducing atmosphere. The $p(O_2)$ dependence of the electron concentration results from eq 5:

$$[e'] \propto p(O_2)^{-1/4} \quad (6)$$

Assuming constant mobility μ_i of the carriers with charge q_i, the partial conductivity σ_i is directly proportional to the defect concentration c_i ($\sigma_i = q_i\mu_i c_i$) and reflects the oxygen partial pressure dependence of c_i. As shown in Figure 6, the total conductivity of the mesoporous YSZ thin films does not reveal $p(O_2)$ dependence. This means that the electronic contribution to the total conductivity is negligible and the ionic transport via oxygen vacancies is the dominating transport mechanism in the films under dry conditions. The same behavior is known for dense films and single crystals of YSZ.[14,45] From this we conclude that the mesoporous morphology has apparently no effect on the major charge transport mechanism. It should be noted, though, that this conclusion is not necessarily true in general. The high surface area of mesoporous materials may have significant influence on the dominating charge transport mechanism, as recently shown by Hartmann et al.[35] They studied the total conductivity of solid solution thin films of CeO_2 and ZrO_2 as a function of oxygen partial pressure and observed a $p(O_2)$ dependence of the conductivity, with slopes varying between −1/3 and −1/2 depending on the composition. These unusual slopes were explained by a defect model which includes surface defects with different effective charges compared to bulk defects. They also discussed the formation of defect associates.

Although the $p(O_2)$ dependence of the total conductivity of the mesoporous YSZ thin films shows no clear indications of defect associates, their formation may explain the change in slope of conductivity with temperature (see Figure 5).[51] A similar behavior, with two different activation energies, has already been observed for single crystals and polycrystalline YSZ.[52−55] At low temperatures or high doping concentrations, free oxygen vacancies can be trapped at Y'_{Zr} impurities due to Coulomb interaction and form a defect pair:[52−54]

$$Y'_{Zr} + V^{\cdot\cdot}_O \rightleftharpoons (Y'_{Zr} - V^{\cdot\cdot}_O)^{\cdot} \quad (7)$$

As shown by Kilner et al., the formation of defect associates strongly affects the free vacancy concentration, which determines the ionic conductivity.[51] At high temperatures, where the defect pairs dissociate, the activation energy corresponds to the migration enthalpy ΔH_m of the free vacancies. At low temperatures, the binding energy ΔH_a of the defect pairs is included:[56]

$$E_A = \Delta H_m + \Delta H_a \quad (8)$$

As described above, activation energies of 0.78 and 1.28 eV were determined at high and low temperatures, respectively. Consequently, the mesoporous thin films exhibit a migration enthalpy of 0.78 eV. The dissociation enthalpy of the defect associates is about 0.5 eV. These values are comparable to those reported in the literature. Bauerle at al. determined values of ΔH_m = 0.68 eV and ΔH_a = 0.49 eV for single crystals of YSZ,[57] and Filal et al. reported migration enthalpies of 0.65 and 0.89 eV and dissociation enthalpies of 0.5 and 0.22 eV for polycrystals and single crystals, respectively.[54] Apart from the formation of defect associates, other factors, such as additional electronic contribution to the conductivity or increased strain, could in principle also be responsible for the change in activation energy. However, an additional electronic contribution would result in a change of the total conductivity with varying oxygen partial pressure (see eq 6), which is not observed. Also, strain in the YSZ lattice as a possible reason can be excluded because the change in activation energy is only

DOI: 10.1021/acsami.5b01001
ACS Appl. Mater. Interfaces 2015, 7, 11792−11801

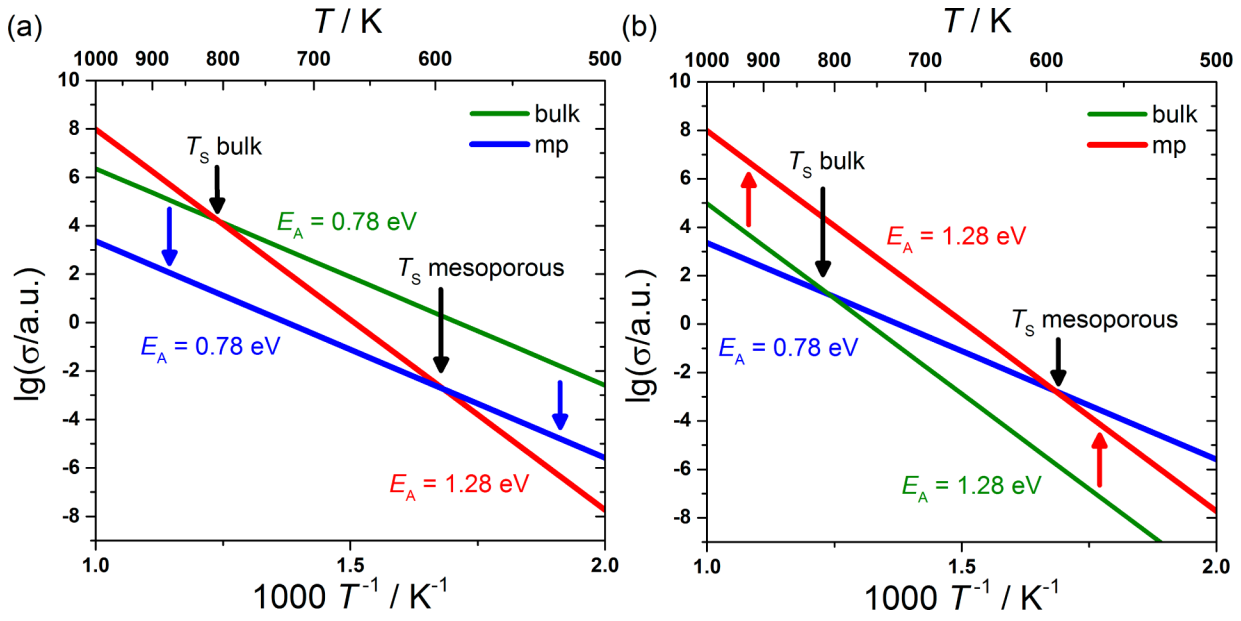

Figure 8. Schematic illustration of two scenarios leading to a shift in T_s to lower temperatures. (a) Conductivity decrease at high temperatures, where the oxygen migration dominates the temperature dependence of the conductivity. (b) Conductivity increase at low temperatures, where the ionic conductivity is dominated by the formation of defect associates.

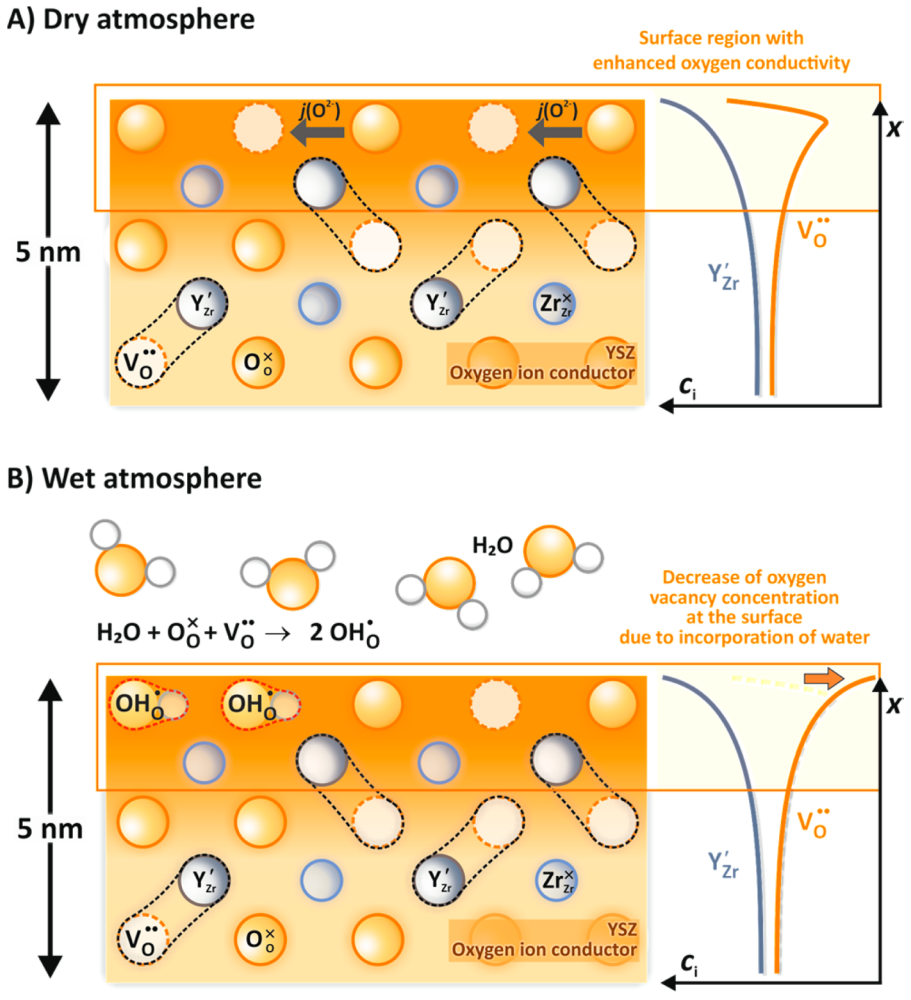

Figure 9. Influence of the surface on the transport properties in mesoporous YSZ. (a) Increased oxygen vacancy concentration leads to enhanced surface conductivity. (b) Formation of hydroxide ions reduces the oxygen vacancy concentration and therefore the surface conductivity.

DOI: 10.1021/acsami.5b01001
ACS Appl. Mater. Interfaces 2015, 7, 11792−11801

observed under dry conditions—strain effects are expected to be independent of atmosphere.

It is interesting to note that the change in slope in the Arrhenius plot is usually observed at temperatures between T_s = 830 and 870 K. However, this transition already occurs at 620 K for the mesoporous films. The shift in T_s to lower temperature can be explained by two possible scenarios, which are schematically illustrated in Figure 8: (a) conductivity decrease at high temperatures, where the oxygen migration dominates the temperature dependence of the conductivity, or (b) conductivity increase at low temperatures, where the ionic conductivity is dominated by the formation of defect associates. In the following, we discuss the latter case as the conductivity is higher in dry atmosphere.

Since bulk and mesoporous YSZ samples show virtually the same activation energy, the increased conductivity at low temperatures can only be attributed to a higher concentration or mobility of the oxygen vacancies, both of which is strongly affected by the formation of space-charge regions at grain boundaries and surfaces. The space charge layer width in YSZ is typically assumed to be 3 nm.[58,59] This is of the order of the grain size. Thus, the total conductivity may be dominated by transport through the space charge region at the surface. Space charge concepts for YSZ assume segregation of yttrium dopants and depletion of oxygen vacancies at grain boundaries.[42,50] However, atomistic simulations predict segregation of oxygen vacancies at the free surface[60]—increased vacancy concentration may be responsible for enhanced surface conductivity (see Figure 9a), thereby resulting in the observed shift in T_s.

The strong influence of the surface on the transport properties of the mesoporous thin films is also observed when the atmosphere is changed from dry to "humid". As previously mentioned, the conductivity decreases by nearly 1 order of magnitude in ambient atmosphere over the whole temperature range investigated. The total conductivity usually increases significantly in humid air at temperatures below 200 °C, which is attributed to proton conduction along the surface[31] or grain boundaries.[27,61] In this case, proton defects are formed in the form of hydroxide ions ($(OH)_O^{\cdot}$) according to the following defect reaction:[62,63]

$$H_2O_{(g)} + V_O^{\cdot\cdot} + O_O^x \rightleftharpoons 2(OH)_O^{\cdot} \quad (9)$$

The hydroxyl groups can persist on the surface of oxide materials up to 500 °C, as shown by Raz et al.[64] But given that proton conduction is negligible compared to oxygen ion conduction at high temperatures,[52,61,65] no significant change in conductivity has been observed in wet air atmosphere for dense YSZ at temperatures above 200 °C, neither for single crystals[52] nor polycrystals[27,31] or thin films.[22] However, because the contribution of proton transport increases with decreasing grain size,[27] proton conduction has been observed up to 400 °C in nanoporous YSZ thin films, as reported by Scherrer et al.[66] Miyoshi et al. observed proton transport in nanograined YSZ even up to 500 °C, which they also attributed to the unique structure of the material and the presence of hydrate layers between the surfaces of adjacent grains.[26,67]

In view of the fact that the mesoporous thin films employed here show no increase in conductivity in ambient atmosphere, the influence of proton transport appears to be small. The onset of proton conduction may be inferred from the data in Figure 5 at low temperatures; the conductivity slightly deviates from the linear fit below ~530 K (250 °C). Overall, this indicates that the amount of adsorbed water is not sufficient to provide additional transport pathways for protons (high proton conduction is usually observed in wet atmosphere). Nevertheless, the significant decrease in conductivity—in ambient atmosphere—can be attributed to the presence of water on the surface of the mesoporous thin films (see Figure 9b). The adsorption of water not only results in the formation of proton defects, but also in the annihilation of oxygen vacancies (see eq 9).[68,69] These vacancies are responsible for the oxygen ion conduction, and thus their annihilation is expected to have a profound effect on the conductivity. For example, a decrease in ionic conductivity by almost 2 orders of magnitude has been observed for hydrated mayenite.[70] This is comparable to what we find for the mesoporous YSZ thin films.

The annihilation of vacancies is clearly limited to the surface because water does not dissolve in cubic YSZ.[68] Therefore, the decrease in conductivity indicates that, on the one hand, a noticeable amount of vacancies (at the free surface of the mesoporous films) is in fact annihilated and the surface transport makes a significant contribution to the total conductivity. On the other hand, the amount of adsorbed water seems insufficient to affect the conductivity due to substantial proton transport. Future work (e.g., humidity dependent conductivity studies) is necessary to confirm these hypotheses and fully explore the mechanism.

CONCLUSIONS

In summary, we have shown that single phase cubic YSZ thin films with an ordered mesoporous morphology can be prepared by sol-gel co-assembly through a soft-templating method using the large diblock copolymer PIB_{107}-*b*-PEO_{150} as structure-directing agent. The nanocrystalline material is well-defined at different length scales and shows no signs of instability at 600 °C. Due to high surface-to-volume ratio (surface phenomena), the films possess unique transport properties compared to bulk YSZ. Under dry air conditions, defect associates are already formed at temperatures below 350 °C. Furthermore, the total conductivity is strongly reduced in ambient atmosphere. This decrease is likely due to water adsorption on the free surface, which is accompanied by the annihilation of oxygen vacancies. Overall, our results demonstrate a significant contribution of the surface region to the total conductivity of the solution-processed mesostructured thin films.

ASSOCIATED CONTENT

Supporting Information

Top view and cross-sectional SEM images, SAED pattern, XPS spectra (survey and O 1s), and Raman data of the mesoporous YSZ thin films; parasitic resistance and capacitance of bare quartz glass substrates; and schematic illustration of the interdigitated Pt electrodes. The Supporting Information is available free of charge on the ACS Publications website at DOI: 10.1021/acsami.5b01001.

AUTHOR INFORMATION

Corresponding Authors

*Phone: +49 641 9934544. E-mail: matthias.elm@exp1.physik.uni-giessen.de.

*Phone: +49 721 60828827. E-mail: torsten.brezesinski@kit.edu.

DOI: 10.1021/acsami.5b01001
ACS Appl. Mater. Interfaces 2015, 7, 11792−11801

Author Contributions

All authors have given approval to the final version of the manuscript. The paper was written through contributions from M.T.E., J.J., and T.B.

Notes

The authors declare no competing financial interest.

■ ACKNOWLEDGMENTS

We thank Dr. C. Reitz (KIT) for SEM and GISAXS, Dr. D. Wang (KIT) for TEM, Dr. M. Rohnke (JLU Giessen) for ToF-SIMS, and Dr. B. Luerßen (JLU Giessen) for help in preparing the figures. Parts of this research were carried out at the light source DORIS III at DESY, a member of the Helmholtz Association (HGF). We would like to thank Dr. J. Perlich for assistance in using beamline BW4. The authors gratefully acknowledge support by the research program LOEWE (project STORE-E) funded by the State of Hessen.

■ REFERENCES

(1) Singhal, S. Advances in Solid Oxide Fuel Cell Technology. *Solid State Ionics* **2000**, *135*, 305−313.
(2) Holtappels, P.; Vogt, U.; Graule, T. Ceramic Materials for Advanced Solid Oxide Fuel Cells. *Adv. Eng. Mater.* **2005**, *7*, 292−302.
(3) Minh, N. Q. Solid Oxide Fuel Cell Technology—Features and Applications. *Solid State Ionics* **2004**, *174*, 271−277.
(4) Park, C.; Akbar, S.; Weppner, W. Ceramic Electrolytes and Electrochemical Sensors. *J. Mater. Sci.* **2003**, *38*, 4639−4660.
(5) Kerman, K.; Ramanathan, S. Complex Oxide Nanomembranes for Energy Conversation and Storage: A Review. *J. Mater. Res.* **2014**, *29*, 320−337.
(6) Evans, A.; Bieberle-Hütter, A.; Rupp, J. L.; Gauckler, L. J. Review on Microfabricated Micro-Solid Oxide Fuel Cell Membranes. *J. Power Sources* **2009**, *194*, 119−129.
(7) Minh, N. Q. Ceramic Fuel Cells. *J. Am. Ceram. Soc.* **1993**, *76*, 563−588.
(8) Pihlatie, M.; Kaiser, A.; Mogensen, M.; Redox, M. Stability of SOFC: Thermal Analysis of Ni-YSZ Composites. *Solid State Ionics* **2009**, *180*, 1100−1112.
(9) Tarancón, A. Strategies for Lowering Solid Oxide Fuel Cells Operating Temperature. *Energies* **2009**, *2*, 1130−1150.
(10) Wachsman, E. D.; Lee, K. T. Lowering the Temperature of Solid Oxide Fuel Cells. *Science* **2011**, *334*, 935−939.
(11) Tuller, H. L. Ionic Conduction in Nanocrystalline Materials. *Solid State Ionics* **2000**, *131*, 143−157.
(12) Jiang, J.; Hertz, J. On the Variability of Reported Ionic Conductivity in Nanoscale YSZ Thin Films. *J. Electroceram.* **2014**, *32*, 37−46.
(13) Zhang, Y. W.; Jin, S.; Yang, Y.; Li, G. B.; Tian, S. J.; Jia, J. T.; Liao, C. S.; Yan, C. H. Electrical Conductivity Enhancement in Nanocrystalline $(RE_2O_3)_{0.08}(ZrO_2)_{0.92}$ (RE = Sc,Y) Thin Films. *Appl. Phys. Lett.* **2000**, *77*, 3409−3411.
(14) Kosacki, I.; Suzuki, T.; Petrovsky, V.; Anderson, H. U. Electrical Conductivity of Nanocrystalline Ceria and Zirconia Thin Films. *Solid State Ionics* **2000**, *136*, 1225−1233.
(15) Karthikeyan, A.; Chang, C.-L.; Ramanathan, S. High Temperature Conductivity Studies on Nanoscale Yttria-doped Zirconia Thin Films and Size Effects. *Appl. Phys. Lett.* **2006**, *89*, 183116.
(16) Sillassen, M.; Eklund, P.; Pyrds, N.; Johnson, E.; Helmersson, U.; Bøttiger, J. Low Temperature Superionic Conductivity in Strained Yttria-Stabilized Zirconia. *Adv. Funct. Mater.* **2010**, *20*, 2071−2076.
(17) Schichtel, N.; Korte, C.; Hesse, D.; Janek, J. Elastic Strain at Interfaces and its Influence on Ionic Conductivity in Nanoscaled Solid Electrolyte Thin Films—Theoretical Considerations and Experimental Studies. *Phys. Chem. Chem. Phys.* **2009**, *11*, 3043−3048.
(18) Jiang, J.; Hu, X.; Shen, W.; Ni, C.; Hertz, J. L. Improved Ionic Conductivity in Strained in Yttria-Stabilized Zirconia Thin Films. *Appl. Phys. Lett.* **2013**, *102*, 143901.
(19) Kosacki, I.; Rouleau, C. M.; Becher, P. F.; Bentley, J.; Lowndes, D. H. Nanoscale Effect on the Ionic Conductivity in Highly Textured YSZ Thin Films. *Solid State Ionics* **2005**, *176*, 1319−1326.
(20) Rivera, A.; Santamaria, J.; León, C. Electrical Conductivity Relaxation in Thin-Film Yttria-Stabilized Zirconia. *Appl. Phys. Lett.* **2001**, *78*, 610−612.
(21) Gerstl, M.; Navickas, E.; Friedbacher, G.; Kubel, F.; Ahrens, M.; Fleig, J. The Separation of Grain and Grain Boundary Impedance in Thin Yttria Stabilized Zirconia (YSZ) Layers. *Solid State Ionics* **2011**, *185*, 32−41.
(22) Guo, X.; Vasco, E.; Mi, S.; Szot, K.; Wachsman, E.; Waser, R. Ionic Conduction in Zirconia Thin Films of Nanometer Thickness. *Acta Mater.* **2005**, *53*, 5161−5166.
(23) Navickas, E.; Gerstl, M.; Kubel, F.; Fleig, J. Simultaneous Measurement of the In- and Across-Plane Ionic Conductivity of YSZ Thin Films Fuel Cells and Energy Conversion. *J. Electrochem. Soc.* **2012**, *159*, B411−B416.
(24) Kim, S.; Anselmi-Tamburini, U.; Park, H.; Martin, M.; Munir, Z. Unprecedented Room-Temperature Electrical Power Generation Using Nanoscale Fluorite-Structured Oxide Electrolytes. *Adv. Mater.* **2008**, *20*, 556−559.
(25) Gregori, G.; Shirpour, M.; Maier, J. Proton Conduction in Dense and Porous Nanocrystalline Ceria Thin Films. *Adv. Funct. Mater.* **2013**, *23*, 5861−5867.
(26) Miyoshi, S.; Akao, Y.; Kuwata, N.; Kawamura, J.; Oyama, Y.; Yagi, T.; Yamaguchi, S. Water Uptake and Conduction Property of Nano-grained Yttria-doped Zirconia Fabricated by Ultra-High Pressure Compaction at Room Temperature. *Solid State Ionics* **2012**, *207*, 21−28.
(27) Avila-Paredes, H. J.; Zhao, J.; Wang, S.; Pietrowski, M.; De Souza, R. A.; Reinholdt, A.; Munir, Z. A.; Martin, M.; Kim, S. Protonic Conductivity of Nano-structured Yttria-stabilized Zirconia: Dependence on Grain Size. *J. Mater. Chem.* **2010**, *20*, 990−994.
(28) Pérez-Coll, D.; Sánchez-López, E.; Mather, G. C. Influence of Porosity on the Bulk and Grain-Boundary Electrical Properties of Gd-doped Ceria. *Solid State Ionics* **2010**, *181*, 1033−1042.
(29) Pietrowski, M. J.; De Souza, R. A.; Kim, S.; Munir, Z. A.; Martin, M. Dehydration Kinetics of Nano-YSZ Ceramics Monitored by In-situ Infrared Spectroscopy. *Solid State Ionics* **2012**, *225*, 241−244.
(30) Avila-Paredes, H. J.; Barrera-Calva, E.; Anderson, H. U.; De Souza, R. A.; Martin, M.; Munir, Z. A.; Kim, S. Room-Temperature Protonic Conduction in Nanocrystalline Films of Yttria-Stabilized Zirconia. *J. Mater. Chem.* **2010**, *20*, 6235−6238.
(31) Tandé, C.; Perez-Coll, D.; Mather, G. C. Surface Proton Conductivity of Dense Nanocrystalline YSZ. *J. Mater. Chem.* **2012**, *22*, 11208−11213.
(32) Korte, C.; Keppner, J.; Peters, A.; Schichtel, N.; Aydin, H.; Janek, J. Coherency Strain and its Effect on Ionic Conductivity and Diffusion in Solid Electrolytes—An Improved Model for Nanocrystalline Thin Films and a Review of Experimental Data. *Phys. Chem. Chem. Phys.* **2014**, *16*, 24575−24591.
(33) Wang, J.; Polleux, J.; Lim, J.; Dunn, B. Pseudocapacitive Contributions to Electrochemical Energy Storage in TiO_2 (Anatase) Nanoparticles. *J. Phys. Chem. C* **2007**, *111*, 14925−14931.
(34) Hartmann, P.; Lee, D.-K.; Smarsly, B. M.; Janek, J. Mesoporous TiO_2: Comparison of Classical Sol-Gel and Nanoparticle Based Photoelectrodes for the Water Splitting Reaction. *ACS Nano* **2010**, *4*, 3147−3154.
(35) Hartmann, P.; Brezesinski, T.; Sann, J.; Lotnyk, A.; Eufinger, J.-P.; Kienle, L.; Janek, J. Defect Chemistry of Oxide Nanomaterials with High Surface Area: Ordered Mesoporous Thin Films of the Oxygen Storage Catalyst CeO_2−ZrO_2. *ACS Nano* **2013**, *7*, 2999−3013.
(36) Brinker, C. J.; Lu, Y.; Sellinger, A.; Fan, H. Evaporation-Induced Self-Assembly: Nanostructures Made Easy. *Adv. Mater.* **1999**, *11*, 579−585.
(37) Crepaldi, E. L.; Soler-Illia, G. J. D. A.; Bouchara, A.; Grosso, D.; Durand, D.; Sanchez, C. Controlled Formation of Highly Ordered Cubic and Hexagonal Mesoporous Nanocrystalline Yttria-Zirconia and

DOI: 10.1021/acsami.5b01001
ACS Appl. Mater. Interfaces 2015, 7, 11792−11801

Ceria-Zirconia Thin Films Exhibiting High Thermal Stability. *Angew. Chem., Int. Ed.* **2003**, *42*, 347−351.
(38) Lu, Y.; Ganguli, R.; Drewien, C. A.; Anderson, M. T.; Brinker, C. J.; Gong, W.; Guo, Y.; Soyez, H.; Dunn, B.; Huang, M. H.; Zink, J. I. Continuous Formation of Supported Cubic and Hexagonal Mesoporous Films by Sol Gel Dip-Coating. *Nature* **1997**, *389*, 364−368.
(39) Weidmann, C.; Brezesinski, K.; Suchomski, C.; Tropp, K.; Grosser, N.; Haetge, J.; Smarsly, B. M.; Brezesinski, T. Morphology-Controlled Synthesis of Nanocrystalline eta-Al_2O_3 Thin Films, Powders, Microbeads, and Nanofibers with Tunable Pore Sizes from Preformed Oligomeric Oxo-Hydroxo Building Blocks. *Chem. Mater.* **2012**, *24*, 486−494.
(40) Reitz, C.; Haetge, J.; Suchomski, C.; Brezesinski, T. Facile and General Synthesis of Thermally Stable Ordered Mesoporous Rare-Earth Oxide Ceramic Thin Films with Uniform Mid-Size to Large-Size Pores and Strong Crystalline Texture. *Chem. Mater.* **2013**, *25*, 4633−4642.
(41) Cai, J.; Raptis, C.; Raptis, Y. S.; Anastassakis, E. Temperature Dependence of Raman Scattering in Stabilized Cubic Zirconia. *Phys. Rev. B* **1995**, *51*, 201−209.
(42) Guo, X.; Zhang, Z. Grain Size Dependent Grain Boundary Defect Structure: Case of Doped Zirconia. *Acta Mater.* **2003**, *51*, 2539−2547.
(43) Fleig, J. The Grain Boundary Impedance of Random Microstructures: Numerical Simulations and Implications for the Analysis of Experimental Data. *Solid State Ionics* **2002**, *150*, 181−193.
(44) Irvine, J. T. S.; Sinclair, D. C.; West, A. R. Electroceramics: Characterization by Impedance Spectroscopy. *Adv. Mater.* **1990**, *2*, 132−138.
(45) Park, J.; Blumenthal, R. N. Electronic Transport in 8 Mole Percent Y_2O_3−ZrO_2. *J. Electrochem. Soc.* **1989**, *136*, 2867−2876.
(46) Ikeda, S.; Sakurai, O.; Uematsu, K.; Mizutani, N.; Kato, M. Electrical Conductivity of Yttria-stabilized Zirconia Single Crystals. *J. Mater. Sci.* **1985**, *20*, 4593−4600.
(47) Joo, J. H.; Choi, C. M. Electrical Conductivity of YSZ Film Grown by Pulsed Laser Deposition. *Solid State Ionics* **2006**, *177*, 1053−1057.
(48) Kosacki, I.; Anderson, H. U. Microstructure−Property Relationships in Nanocrystalline Oxide Thin Films. *Ionics* **2000**, *6*, 294.
(49) Gleiter, H. Nanostructured Materials: Basic Concepts and Microstructure. *Acta Mater.* **2000**, *48*, 1−29.
(50) Guo, X. Physical Origin of the Intrinsic Grain-Boundary Resistivity of Stabilized-Zirconia: Role of the Space-Charge Layers. *Solid State Ionics* **1995**, *81*, 235−242.
(51) Kilner, J.; Waters, C. The Effects of Dopant Cation-Oxygen Vacancy Complexes on the Anion Transport Properties of Non-Stoichiometric Fluorite Oxides. *Solid State Ionics* **1982**, *6*, 253−259.
(52) Manning, P.; Sirman, J.; De Souza, R. D.; Kilner, J. The Kinetics of Oxygen Transport in 9.5 mol% Single Crystal Yttria Stabilised Zirconia. *Solid State Ionics* **1997**, *100*, 1−10.
(53) Kosacki, I.; Petrovsky, V.; Anderson, H. U. Modeling and Characterization of Electrical Transport in Oxygen Conducting Solid Electrolytes. *J. Electroceram.* **2000**, *4*, 243−249.
(54) Filal, M.; Petot, C.; Mokchah, M.; Chateau, C.; Carpentier, J. Ionic Conductivity of Yttrium-doped Zirconia and the "Composite Effect". *Solid State Ionics* **1995**, *80*, 27−35.
(55) Badwal, S. Electrical Conductivity of Single Crystal and Polycrystalline Yttria-Stabilized zirconia. *J. Mater. Sci.* **1984**, *19*, 1767−1776.
(56) Kilner, J.; Steele, B. C. H. Chapter 5—Mass Transport in Anion-Deficient Fluorite Oxides. In *Nonstoichiometrie in Oxides*; Søerensen, O. T., Ed.; Academic Press: New York, 1981; pp 233−269.
(57) Bauerle, J.; Hrizo, J. Interpretation of the Resistivity Temperature Dependence of High Purity $(ZrO_2)_{0.90}(Y_2O_3)_{0.10}$. *J. Phys. Chem. Solids* **1969**, *30*, 565.
(58) Guo, X.; Maier, J. Grain Boundary Blocking Effect in Zirconia: A Schottky Barrier Analysis. *J. Electrochem. Soc.* **2001**, *148*, E121−E126.
(59) Guo, X.; Waser, R. Space Charge Concept for Acceptor-doped Zirconia and Ceria and Experimental Evidences. *Solid State Ionics* **2004**, *173*, 63−67.
(60) Lee, H. B.; Prinz, F. B.; Cai, W. Atomistic Simulations of Surface Segregation of Defects in Solid Oxide Electrolytes. *Acta Mater.* **2010**, *58*, 2197−2206.
(61) Kim, S.; Avila-Peredes, H. J.; Wang, S.; Chen, C.-T.; De Souza, R. A.; Martin, M.; Munir, Z. A. On the Conduction Pathway for Protons in Nanocrystalline Yttria-Stabilized Zirconia. *Phys. Chem. Chem. Phys.* **2009**, *11*, 3035−3038.
(62) De Souza, R. A.; Munir, Z. A.; Kim, S.; Martin, M. Defect Chemistry of Grain Boundaries in Proton-conducting Solid Oxides. *Solid State Ionics* **2011**, *196*, 1−8.
(63) Guo, X.; He, J. Grain Size Dependent Grain Boundary Defect Structure: Case of Doped Zirconia. *Acta Mater.* **2003**, *51*, 5123−5130.
(64) Raz, S.; Sasaki, K.; Maier, J.; Riess, I. Characterization of Adsorbed Water Layers on Y_2O_3-Doped ZrO_2. *Solid State Ionics* **2001**, *143*, 181−204.
(65) Wagner, C. Solubility of Vapor in ZrO_2-Y_2O_3 Mixed Crystals. *Ber. Bunsen-Ges.- Phys. Chem. Chem. Phys.* **1968**, *72*, 778−781.
(66) Scherrer, B.; Schlupp, M. V.; Stender, D.; Martynczuk, J.; Grolig, J. G.; Ma, H.; Kocher, P.; Lippert, T.; Prestat, M.; Gauckler, L. J. On Proton Conductivity in Porous and Dense Yttria Stabilized Zirconia at Low Temperature. *Adv. Funct. Mater.* **2013**, *23*, 1957−1964.
(67) Miyoshi, S.; Akao, Y.; Kuwata, N.; Kawamura, J.; Oyama, Y.; Yagi, T.; Yamaguchi, S. Low-Temperature Protonic Conduction Based on Surface Protonics: An Example of Nanostructured Yttria-Doped Zirconia. *Chem. Mater.* **2014**, *26*, 5194−5200.
(68) Guo, X. Low Temperature Stability of Cubic Zirconia. *Phys. Status Solidi A* **2000**, *177*, 191−201.
(69) Guo, X. On the Degradation of Zirconia Ceramics during Low-Temperature Annealing in Water or Water Vapor. *J. Phys. Chem. Solids* **1999**, *60*, 539−546.
(70) Lee, D.-K.; Kogel, L.; Ebbinghaus, S. G.; Valov, I.; Wiemhoefer, H.-D.; Lerch, M.; Janek, J. Defect Chemistry of the Cage Compound, $Ca_{12}Al_{14}O_{33-\delta}$—Understanding the Route from a Solid Electrolyte to a Semiconductor and Electride. *Phys. Chem. Chem. Phys.* **2009**, *11*, 3105−3114.

DOI: 10.1021/acsami.5b01001
ACS Appl. Mater. Interfaces 2015, 7, 11792−11801